

A Computational Study of High-Speed Microdroplet Impact onto a Smooth Solid Surface

J. Q. Feng

Optomec, Inc., 2575 University Avenue, Suite 135, St. Paul, Minnesota 55114, USA

Email: jfeng@optomec.com

(Received April 20, 2016; accepted September 23, 2016)

ABSTRACT

Numerical solutions of high-speed microdroplet impact onto a smooth solid surface are computed, using the *interFoam* VoF solver of the OpenFOAM[®] CFD package. Toward the solid surface, the liquid microdroplet is moving with an impinging gas flow, simulating the situation of ink droplets being deposited onto substrate with a collimated mist jet in the Optomec Aerosol Jet[®] printing process. For simplicity and computational efficiency, axisymmetric incompressible flow is assumed here for the free-surface fluid dynamic problem. The computed values of maximum spread factor ζ , for the range of parameters relevant to Aerosol Jet[®] printing, are found in good agreement with some of the correlation formulas proposed by previous authors in the literature. A formula of improved accuracy is then obtained for evaluating ζ of Aerosol Jet[®] deposited droplets, by combining selected formulas from different authors with appropriate modifications. The computational results also illustrate droplet impact dynamics with lamella shape evolution throughout the spreading, receding-relaxation, and wetting equilibrium phases, consistent with that observed and described by many authors. This suggests a scale-invariant nature of the basic droplet impact behavior such that experiments with larger droplets at the same nondimensional parameter values may be applicable for studying microdroplet impact dynamics. Significant free surface oscillations can be observed with low viscosity droplets. The border line between free surface oscillations and aperiodic creeping to the capillary equilibrium shape appears at $Oh \sim 0.25$. Droplet bouncing after receding is prompted with large contact angles at solid surface (as consistent with findings reported in the literature), but can be suppressed by increasing the droplet viscosity.

Keywords: Drop impact; Microdroplet; Aerosol Jet[®]; Volume-of-fluid (VoF); Computational analysis.

NOMENCLATURE

Ca	capillary number	α	phase fraction function
d	droplet diameter	γ	surface tension
H	center height of free surface (in units of d)	μ_d	droplet liquid viscosity
Oh	Ohnesorge number	μ_g	gas viscosity
R	contact radius of free surface on solid surface (in units of d)	ζ	maximum spread factor
Re	Reynolds number	θ_0	static contact angle
U	velocity of gas impinging flow	θ_A	leading edge contact angle
We	Weber number	θ_R	trailing edge contact angle
		ρ_d	droplet liquid density
		ρ_g	gas density

1. INTRODUCTION

With the Aerosol Jet[®] direct-write technology, ink microdroplets generated by a liquid atomization process are deposited onto a substrate in a form of collimated mist stream (which can become less than 10 μm in diameter having the ink mist concentration typically about 50 nL/cc) with

considerable impinging velocity, e.g., 20 to 100 m/s (cf. Renn, 2006; Zollmer *et al.*, 2006; Hedges *et al.*, 2007; Kahn, 2007; Renn *et al.*, 2010; Christenson *et al.*, 2011; Paulsen *et al.*, 2012). Therefore, the ink mist can have sufficient momentum to impact the substrate several millimeters away from the deposition nozzle as directed by the high-speed jet flow (cf. Feng, 2015). The Aerosol Jet[®] functional

Inks typically consist of suspensions of nanoparticles or polymer solutions formulated with appropriate properties such that they can be adequately aerosolized with a liquid atomizer. The ink droplet diameter is usually in a narrow range of 1 to 5 μm with the volume mean diameter around 2.5 μm , such that fine features as small as $\sim 10 \mu\text{m}$ can be produced by the additive manufacturing process. As with many industrial applications such as spray coating, inkjet printing, and so forth, understanding of droplet deposition behavior is important for achieving desired Aerosol Jet[®] print quality. Therefore, a detailed analysis of high-speed microdroplet impact on a solid surface can provide practically valuable insights.

The process of droplet impact on a surface involves various free-surface fluid dynamics phenomena, ranging from spreading, receding, oscillating, to bouncing, splashing, etc. (Yarin, 2006). It has been a subject of intensive study by many authors (e.g., Ford and Furnidge, 1967; Foote, 1974; Chandra and Avedisian, 1991; Rein, 1993; Healy *et al.*, 1996; Busmann *et al.*, 1999, 2000; Sikalo *et al.*, 2002; Rioboo *et al.*, 2001, 2002; Toivakka, 2003; Law, 2015, as well as references cited therein), for its relevance to a wide variety of applications. Yet, our understanding of the associated fluid dynamics may still be far from thorough, probably due to the difficulties in consistent characterizations of wetting and surface properties as well as lack of agreeable formulations of moving contact line boundary conditions for theoretical modeling. For example, numerous empirical and semi-empirical formulas were proposed for describing the maximum spread factor, defined as the maximum normalized contact diameter of the lamella at the end of spreading phase, for its practical importance (e.g., Scheller and Bousfield, 1995; Pasandideh-Fard *et al.*, 1996; Toivakka, 2003; Attane *et al.*, 2007; Roisman, 2009; German and Bertola, 2009); each has an apparently different form and quantitative agreement with each other for a given case usually does not seem as good as one would hope (cf. Perelaer *et al.*, 2009; Ravi *et al.*, 2010; Visser *et al.*, 2012, 2015). This makes it very difficult to determine which formula to use for estimating the spot size as a result of deposition of each individual ink droplet on the substrate with parameters of interest.

Because the Aerosol Jet[®] printing process involves micron-size droplets carried by a high-speed impinging gas jet at velocity typically around 50 m/s, experimental investigations can be quite challenging and prohibitively expensive, if not impossible. Rather recently Visser *et al.* (2012, 2015) have reported experimental measurements of microdroplet impact with an interferometric technique that enabled sub-micron spatial resolution at frame rates exceeding 10^7 per second, which still seems to be an order of magnitude short for the Aerosol Jet[®] situation. To date, computational analysis with numerical solutions of the governing equations may be the only option for gaining insights into the microdroplet impact at high velocity relevant to the Aerosol Jet[®] additive

manufacturing process.

Due to extensive free surface deformations involved in droplet impact process, numerical computations have remained challenging. Although the explicit interface tracking method with boundary-fitted moving mesh using an arbitrary Lagrangian-Eulerian scheme offers the highest accuracy for the free-surface flow problem, it is usually effective for the types of problems with moderate free surface deformations without topology changes (e.g., Feng, 2010, 2015) and becomes too complicated to be practically applicable to the situation of droplet impact problem where phase topology can change with significant free surface movement or even disintegration. On the other hand, the implicit Eulerian interface capturing methods such as volume of fluid (VoF) have been developed for effective computations of flows involving substantial topology changes with interface breaking (because the mesh does not need to move with the interface), despite some compromise of numerical accuracy. Among many versions of the VoF solvers, the *interFoam* of an open-source CFD package called OpenFOAM[®] has been attractive to numerous users and validated by many authors (Berberovic *et al.*, 2009; Saha and Mitra, 2009; Deshpande *et al.*, 2012; Morgan, 2013; Hoang *et al.*, 2013). Over years of code development and testing, the numerical algorithms implemented in *interFoam* have been continuously improved to enable reasonably accurate interface representation with effective advection treatment, handling large density ratios, reducing “spurious (parasitic) currents”, and so forth (Gopala and van Wachem, 2008; Deshpande *et al.*, 2012). The VoF method has also been used to include effects of heat transfer and phase change in simulations of the semi-molten particle impact problem (Alavi *et al.*, 2012).

The purpose of the present work is to compute axisymmetric solutions of a droplet impact on a solid surface with parameters relevant to the Aerosol Jet[®] printing, using the well-established *interFoam* VoF solver. Through detailed comparisons of the computed results with the available formulas from previous authors, an accurate formula for the maximum spread factor can be assembled for predicting the deposition spot size on substrate due to an isolated individual droplet impact. Such spot sizes directly relate to achievable resolutions with the ink droplet size distribution involved in Aerosol Jet[®] printing. Moreover, the numerical solutions can also reveal other possible outcomes beyond spreading phase, such as oscillations, bouncing, etc. In what follows, section 2 briefly describes the computational method, section 3 presents the numerical results for various *We*, with implications for Aerosol Jet[®] printing discussed in section 4 and concluding remarks provided in section 5.

2. COMPUTATIONAL METHOD

Considered here is a liquid droplet of density ρ_d , viscosity μ_d , surface tension γ , and diameter d impacting a smooth solid surface as carried by a gas

impinging flow at velocity U (Fig. 1). The surrounding gas has density ρ_g and viscosity μ_g . Solutions to the Navier-Stokes equations for incompressible Newtonian fluids are computed using the *interFoam* VoF solver of the OpenFOAM® CFD package.

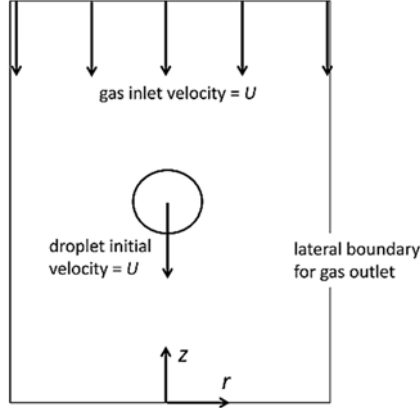


Fig. 1. Schematics of a droplet moving with impinging gas flow at velocity U to impact a solid surface.

With the volume-of-fluid (VoF) method, an indicator function α (also called the phase fraction function) is used to represent the volume fraction of one of the phases. The discontinuity at a gas-liquid interface is represented by a gradient of the continuous function α . Therefore, the interface is rendered as a diffuse layer with finite thickness on the order of the finite volume cell size, and the interface location may not be determined precisely with sub-grid resolution. Two immiscible fluids are treated as one effective fluid throughout the problem domain, having a continuously distributed phase fraction function α ($0 \leq \alpha \leq 1$) as well as distributed density ρ and viscosity μ according to

$$\rho \equiv \rho_d \alpha + \rho_g (1 - \alpha) \text{ and } \mu \equiv \mu_d \alpha + \mu_g (1 - \alpha). \quad (1)$$

To improve the interface resolution, the transport equation for phase fraction function used in *interFoam* is of the form (Ubbink, 2002; Rusche, 2002; Berberovic *et al.*, 2009)

$$\frac{\partial \alpha}{\partial t} + \nabla \cdot (\alpha \mathbf{u}) + \nabla \cdot [\alpha(1 - \alpha) \mathbf{u}_r] = 0, \quad (2)$$

where the velocity of the effective fluid and relative velocity are respectively

$$\mathbf{u} \equiv \alpha \mathbf{u}_d + (1 - \alpha) \mathbf{u}_g \text{ and } \mathbf{u}_r \equiv \mathbf{u}_d - \mathbf{u}_g.$$

Then, the momentum equation can be written as

$$\begin{aligned} \frac{\partial(\rho \mathbf{u})}{\partial t} + \nabla \cdot (\rho \mathbf{u} \mathbf{u}) - \nabla \cdot (\mu \nabla \mathbf{u}) - (\nabla \mathbf{u}) \cdot \nabla \mu \\ = -\nabla p - g \mathbf{e}_g \cdot \mathbf{x} \nabla \rho + \gamma \kappa \nabla \alpha, \end{aligned} \quad (3)$$

where γ denotes the interfacial tension and κ the mean curvature of the free interface, determined from

$$\kappa \equiv -\nabla \cdot \left(\frac{\nabla \alpha}{|\nabla \alpha|} \right). \quad (4)$$

In (3), g is the value and \mathbf{e}_g the unit vector of gravitational acceleration, \mathbf{x} is the position vector, and p the lumped (or piezometric) pressure defined as

$$p \equiv p_0 - \rho g \mathbf{e}_g \cdot \mathbf{x},$$

with p_0 denoting the thermodynamic pressure. For incompressible flow, the velocity field also satisfies the continuity equation

$$\nabla \cdot \mathbf{u} = 0. \quad (5)$$

As illustrated in Fig. 1, no-slip boundary condition ($\mathbf{u} = 0$) is applied at the solid surface ($z = 0$), and a uniform-fixed-value velocity ($\mathbf{u} = -U \mathbf{e}_z$) is specified at the inlet ($z = 10 \times d$), where \mathbf{e}_z denotes the unit normal vector in z -direction. At the outlet ($r = 5 \times d$), a fixed-value pressure is specified with the *pressureInletOutletVelocity* boundary condition for flow velocity. At the three-phase contact line, the *dynamicAlphaContactAngle* condition according to

$$\theta = \theta_0 + (\theta_A - \theta_R) \tanh(u_w / u_\theta) \quad (6)$$

is used with the static contact angle θ_0 , leading edge contact angle θ_A , trailing edge contact angle θ_R , and velocity scaling u_θ being specified. The contact line moving velocity along the solid wall is denoted by u_w in (6), which becomes part of the solution when specifying the contact angle condition related to $\nabla \alpha$ at the contact line that is implicitly allowed to move (or “slip”) in the local cell (cf. Saha and Mitra, 2009; Linder *et al.*, 2013). Without complete agreement on the boundary conditions to be implemented at the moving contact line for modeling (Yarin, 2006), the parameter values for *dynamicAlphaContactAngle* are selected somewhat arbitrarily in the present work only for demonstrating the possible fluid dynamics phenomena.

More often than not in Aerosol Jet® operations, the collimated mist stream is arranged to impinge perpendicularly onto the substrate. With the mist stream wrapped in a thick gas sheath and substrate typically located more than $10 \times$ the nozzle diameter away from nozzle exit, the individual ink droplets can be reasonably assumed to impact substrate perpendicularly with negligible deviations. Because the relevant droplet impact problem can be simplified to an axisymmetric configuration with a simple rectangular domain as shown in Fig. 1, a mesh with wedge cells is generated with the *blockMesh* utility to take advantage of axisymmetry. To ensure adequate resolution of the droplet free surface profile, the impaction region contains finite volume quadrilateral cells with side length less than $0.01 \times d$ (comparable to that used by Toivakka, 2003; Dinc and Gray, 2012, for VoF computations of drop impact problems). Initial position of the droplet center is set at $5 \times d$ with the droplet initial velocity set as the impinging gas jet velocity U , using the *funkySetFields* utility of

swak4foam with OpenFOAM®.

For the nominal setting, the surrounding gas (e.g., nitrogen—the typical mist carrier gas used in Aerosol Jet® process—under ambient temperature and pressure) is assumed to have $\rho_g = 1.2 \text{ kg m}^{-3}$ and $\mu_g = 1.8 \times 10^{-5} \text{ N s m}^{-2}$, whereas the liquid droplet typically have $\rho_d = 2 \times 10^3$ (but may vary between 1×10^3 and 4×10^3) kg m^{-3} and μ_d in a range between 1×10^{-3} and 1 N s m^{-2} , representing the typical inks used in Aerosol Jet® printing. The surface tension of the droplet γ is assumed to be constant with a nominal value of 0.04 (but may vary between 0.02 and 0.08) N m^{-1} .

As usual in fluid dynamics analysis, nondimensional parameters can be conveniently utilized. If ρ and μ are respectively measured in units of ρ_d and μ_d , length in units of d , velocity in units of U , time in units of d/U , and pressure in units of $\mu_d U/d$, three parameters would appear in the nondimensionalized (3) such as the Reynolds number $Re \equiv \rho_d U d / \mu_d$ in front of the first and second terms on left side, the inverse capillary number $1/Ca \equiv \gamma / (\mu_d U)$ in place of γ and $\rho_d g d^2 / (\mu_d U) \equiv Bo/Ca$ in place of g on right side, with Bo denoting the Bond number $\rho_d g d^2 / \gamma$. Because the value of Bo/Ca (as the ratio of the terminal velocity under gravity and impacting velocity U) even for a droplet of $d = 10^{-5} \text{ m}$, $\rho_d = 5 \times 10^3 \text{ kg m}^{-3}$ and $\mu_d = 10^{-3} \text{ N s m}^{-2}$ at $U = 10 \text{ m/s}$ with $g = 9.81 \text{ m s}^{-2}$ is $< 5 \times 10^{-3}$, the effect of gravity in Aerosol Jet® ink droplet deposition (where U is typically $> 20 \text{ m/s}$) should be rather negligible. Thus, only Re ($\equiv \rho_d U d / \mu_d$) and Ca ($\equiv \mu_d U / \gamma$) need to be specified as independent parameters in computing numerical solutions.

3. NUMERICAL RESULTS

Since the diameter of ink droplets rarely exceeds $5 \text{ }\mu\text{m}$ in Aerosol Jet® printing, we start by examining cases with a droplet of $d = 5 \text{ }\mu\text{m}$, $\rho_d = 2 \times 10^3 \text{ kg m}^{-3}$, $\mu_d = 10^{-3} \text{ N s m}^{-2}$ (or 1 cp). As a reference, at $U = 100 \text{ m/s}$ (which represents the high end of mist jet velocity in Aerosol Jet® printing) and $\gamma = 0.04 \text{ N m}^{-1}$, the value of Re and Ca are 1000 and 2.5, respectively. When studying the droplet impact problem, many authors often refer to the Weber number $We \equiv \rho_d U^2 d = Re Ca$ and the Ohnesorge number $Oh \equiv \mu_d / \sqrt{\rho_d \gamma d} = \sqrt{Ca/Re}$ (Yarin, 2006), which will also be used here as derived dimensionless parameters in discussion. (Among Re , Ca , We , and Oh , once two of them are specified as independent parameters the other two can then be calculated from the specified two.) Corresponding to $Re = 1000$ and $Ca = 2.5$, we have $We = 2500$ and $Oh = 0.05$ which represent cases of low viscosity ink drops of large sizes at high impact velocity relevant to Aerosol Jet® printing. In another extreme with an ink droplet of $d = 1 \text{ }\mu\text{m}$, $\rho_d = 1 \times 10^3 \text{ kg m}^{-3}$, $\mu_d = 0.1 \text{ N s m}^{-2}$ (or 100 cp), the values of Re and Ca for $\gamma = 0.08 \text{ N m}^{-1}$ and impacting at $U = 20 \text{ m/s}$ become 0.2 and 25, yielding $We = 5$ and $Oh = 11.18$. Here, the results with plots are typically presented in terms of dimensionless parameters with length measured in

units of d , velocity in units of U , and time t in units of d/U , for generality. The condition at contact line (6) is specified as a static contact angle θ_0 with $\theta_A = \theta_0 + 5^\circ$, $\theta_R = \theta_0 - 5^\circ$ and $u_\theta = 1 \text{ m/s}$ for *interFoam* computations.

With transient terms discretized using a first-order implicit Euler scheme, the time step is controlled by setting the maximum Courant number to 0.01 (which is much finer than “ < 0.5 ” as recommended by many authors to avoid significant spurious currents). For post processing the numerical results, an open-source multi-platform data analysis package called *ParaView* (available at www.paraview.org) for scientific visualization is used in the present work.

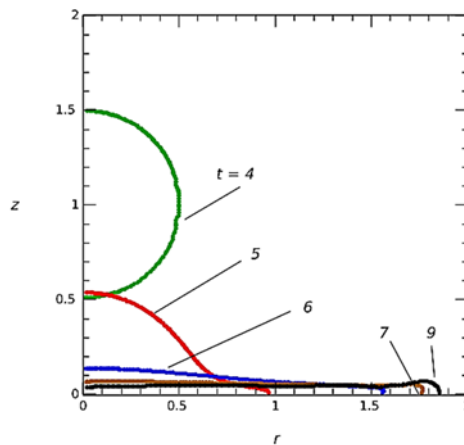


Fig. 2. Spreading: shapes of a droplet of $d = 5 \text{ }\mu\text{m}$, $\rho_d = 2000 \text{ kg m}^{-3}$, and $\mu_d = 1 \text{ cp}$ with $\gamma = 0.04 \text{ N m}^{-1}$, at $U = 100 \text{ m/s}$, with $\theta_0 = 90^\circ$ for time $t = 4, 5, 6, 7$, and 9 (in units of $d/U = 0.05 \text{ }\mu\text{s}$), from $z = 5$ at $t = 0$. The coordinates r and z are labeled in units of d . The free surface profile data came from the output csv file of the ParaView contour for $\alpha = 0.5$.

3.1 Cases of $We = 2500$

Droplets at large We (e.g., $We = 2500$) are expected to have relatively more significant dynamical deformations and to exhibit more dramatic fluid dynamics phenomena. Shown in Fig. 2 are the free surface profiles of a droplet impacting a solid surface and spreading as the contact radius increases with time at $Re = 1000$ and $Ca = 2.5$, for $\theta_0 = 90^\circ$ (with $\theta_A = 95^\circ$, $\theta_R = 85^\circ$, and $u_\theta = 1 \text{ m/s}$). It appears that the droplet has little deformation before impacting the solid surface, because the value of the Weber number based on gas flow $We_g \equiv (\rho_g / \rho_d) \times Re Ca$ is only 1.5, as consistent with the findings of Feng (2010) that noticeable deformations of liquid droplet moving in a gas medium are not expected for $We_g < 5$. Soon after the droplet (with radius of 0.5 in units of d) contacts the solid surface, it spreads to a maximum contact radius about 1.85 at $t \approx 9$ (in units of $d/U = 0.05 \text{ }\mu\text{s}$ for $d = 5 \text{ }\mu\text{m}$ and $U = 100 \text{ m/s}$). It should be noted that the center of droplet is initially located at $z = 5$ at $t = 0$ moving at dimensionless velocity 1 (in units of U) toward the solid surface (at $z = 0$); therefore,

the droplet bottom pole reaches the solid surface around $t = 4.5$. From $t = 4.5$ to 5, the contact line moves from $r = 0$ to $r = 1$ (as indicated in Fig. 2) with an estimated average speed of ~ 2 . Then, the speed of contact line motion is reduced to ~ 0.6 from $t = 5$ to 6 and to ~ 0.2 from $t = 6$ to 7 as the droplet becomes a lamella, and thereafter further down to 0 at $t \approx 9$. The time for spreading process, which is sometimes called the “spreading time” (e.g., Antonini *et al.*, 2012), is $\approx 4.5 \times d/U$ ($= 0.225 \mu\text{s}$).

After spreading to the maximum contact radius, the lamella enters the receding (or relaxation) phase with the contact radius shrinking with time from $t \approx 9$ until $t \approx 80$, as shown in Fig. 3. In the re-ceding process, a growing bulged rim forms around the contact line as it moves toward the center at an average speed of ~ 0.018 , much slower than that in the spreading process. The inner edge of the bulged rim collapse at the center around $t = 44$ and thereafter the droplet center is pushed to move upward quickly. At $t = 55$, the contact line arrives the neighborhood of its equilibrium position $r \approx 0.63$. Because of large $Re = 1000$, the contact radius continues to recede past its equilibrium position toward $r \approx 0.46$ at $t = 80$. At the same time, the upper pole of free surface reaches its maximum height of $z \approx 1.03$.

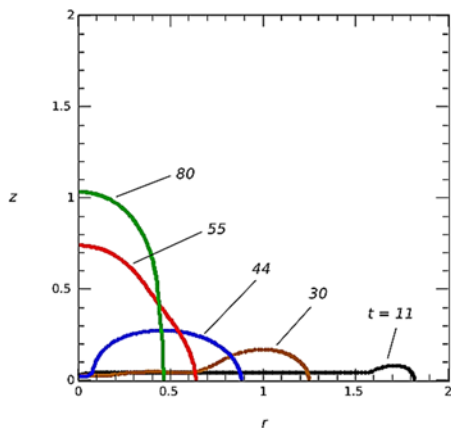


Fig. 3. Receding: as in Fig. 2 but for $t = 11, 30, 44, 55,$ and 80 .

What follows the receding of contact radius is the sessile droplet oscillation up and down around its equilibrium hemispherical shape with a contact radius ≈ 0.63 . Even at $t = 103$ when the contact radius and upper pole are close to their equilibrium value (0.63), the free surface appears to still deviate noticeably from its equilibrium hemispherical shape. But the oscillation amplitude will decay quickly with time by viscous damping, which can clearly be seen in Fig. 5.

The center height H and contact radius R (in units of d) versus time are shown in Fig. 5 for the case of $We = 2500$. When $Re = 1000$ and $Ca = 2.5$ (corresponding to that shown in Figs. 2–4), the droplet exhibits significant oscillations after impaction. Since the initial oscillation amplitude is quite large, the waveform does not appear to be simply sinusoidal (non-sinusoidal oscillations were

also shown in experimental results of Ravi *et al.*, 2010).

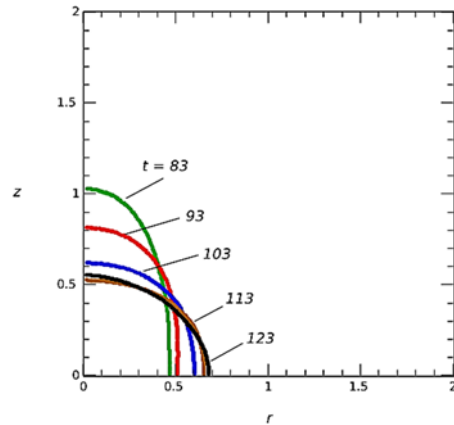


Fig. 4. Oscillating: as in Fig. 2 but for $t = 83, 93, 103, 113,$ and 123 .

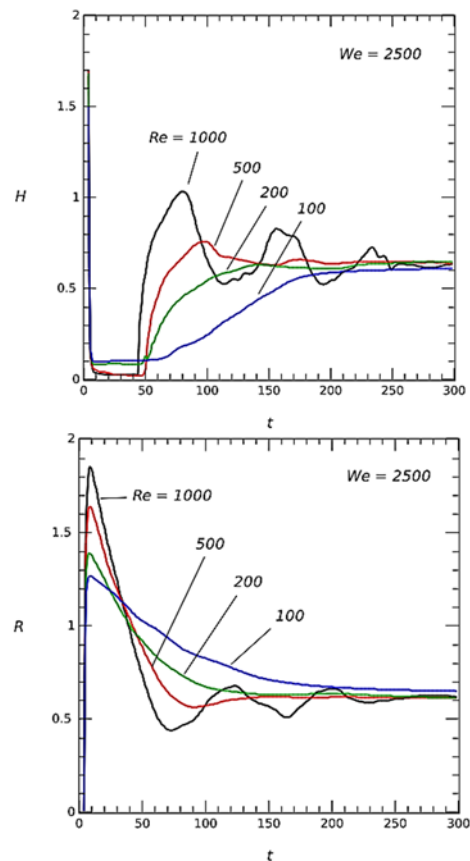


Fig. 5. Plots of the center height H (z -value at $r = 0$ of free surface) and contact radius R (r -value at $z = 0$ of free surface) versus t (in units of $d/U = 0.05 \mu\text{s}$), for droplets of $d = 5 \mu\text{m}$, $\rho_d = 2000 \text{ kg m}^{-3}$, with $\mu_d = 1, 2, 5,$ and 10 cp , at $U = 100 \text{ m/s}$ for $\theta_0 = 90^\circ$.

But the oscillation amplitude decays with time due to viscous damping. If the droplet viscosity is increased to 2 cp (at $Re = 500$ and $Ca = 5$) the amplitude of free surface oscillation diminishes rather quickly due to viscous damping after about one cycle. Oscillations do not seem to occur for μ_d

> 5 cp (for $Oh > 0.25$) indicating the deformed free surface after impactation creeps aperiodically to the equilibrium shape of a hemisphere.

After impactation, the center height H appears to decrease monotonically with t when Re is large reaching its minimum value right before the bulge rim collapse at the center. For example, the values of H_{min} are 0.0266 at $t = 36$ and 0.0231 at $t = 41$ for $Re = 1000$ and 500, respectively. But with reducing the value of Re (corresponding to increasing viscosity μ_d) the value of H_{min} tends to occur at smaller t and then slowly increase. For example, when $Re = 200$ and 100 $H_{min} = 0.0858$ at $t = 9$ and $H_{min} = 0.0998$ at $t = 9$, respectively.

Immediately after the impactation, the contact radius R (which is equivalent to one half of the so-called ‘spread factor’) increases according to a square-root

law, such as $R \propto \sqrt{t^*}$ for $t^* = t - t_0$ with t_0 denoting the time for the impacting droplet to initiate contact to the substrate, typically referred to as the kinematic phase when material points in the droplet mainly move in the z -direction rather than r -direction (Rioboo *et al.*, 2002). For the cases of

$We = 2500$ in Fig. 5, a curve fit of $R = 1.1\sqrt{t^*}$ for $t_0 = 4.51$ appears to be quite accurate for $0 \leq t^* \leq 0.15$, just as expected with the kinematic phase (usually considered for $t^* \ll 1$). As a reference, some fittings of experimental data showed $R = 1.4\sqrt{t^*}$ (Rioboo *et al.*, 2002), yet others had $R = 0.675\sqrt{t^*}$ (e.g., Gupta and Kumar, 2010).

During the kinematic phase, the droplet typically takes the shape of a ‘cut sphere’, similar to that at $t = 5$ in Fig. 2, until a lamella—radially expanding film bounded by a rim—forms in the spreading phase (like the profiles shown in Fig. 2 for $t > 6$). All curves of R versus t in Fig. 5 exhibit a common feature with a quick increase of R immediately after the impact at $t \sim 4.5$ until $t \sim 9$ where R reaches a peak value, and then R decreases with t at a much slower rate. The spreading phase ends when the spreading velocity approaches zero, which usually corresponds to R arriving at its peak value. Following the spreading phase the lamella may begin to recede, which is sometimes called the relaxation phase because the receding contact line now is moving at a relatively much lower speed (as shown in Figs. 3 and 5). After the relaxation phase, the impact kinetic energy is almost dissipated by the viscous effect, and the droplet will go through a slow lengthy ‘wetting equilibrium’ phase (e.g., $R(t) \propto t^{1/10}$ according to Tanner, 1979) toward the capillary equilibrium determined by the static contact angle.

Among many variables involved in droplet impact dynamics, the maximum spread factor $\xi \equiv 2R_{max}$, characterizing the maximum value of contact diameter normalized with the droplet diameter d , has often been considered in the literature for describing the impactation dynamics as well as for comparing results. It can be brought to bear on

various practical applications such as inkjet printing, spray coating, pesticide application, etc. where the actual droplet coverage area directly corresponds to maximum spreading with rapid solidification at contact line, liquid absorption into porous substrate, con-tact line pinning on a textured surface, and so on so forth. According to an empirical correlation by Scheller and Bousfield (1995), it may be expressed as (cf. Yarin, 2006)

$$\xi = 0.61 \times (Re^2 Oh)^{0.166} \quad (7)$$

Another semiempirical relation was proposed by Roisman (2009) which, out of numerous possibilities, is presented here in a modified form as

$$\xi = Re^{1/5} - 0.35 Re^{2/5} / \sqrt{We}, \quad (8)$$

with the original factors 0.87 and 0.40 replaced here by 1.0 and 0.35 for a better match to the values of present computational results.

A comparison of (7) and (8) with the present results is given in Table 1 (for a constant $We = 2500$), which shows remarkably good agreements. As reasonably accurate as they may seem though, neither (7) nor (8) explicitly accounts for the contact angle effect, which was somehow justified by experiments (cf. Scheller and Bousfield, 1995). According to Rioboo *et al.* (2002), immediately after the droplet touches the substrate (and throughout most part of the spreading phase) the contact line motion is controlled by the dominant kinetic energy, irrespective of the physical properties of the liquid and solid such as the contact angle.

Table 1 Comparison of the computed values of ξ with that of (7) and (8) at $We = 2500$ ($U = 100$ m/s), for droplets of $d = 5 \mu\text{m}$, $\rho_d = 2000 \text{ kg m}^{-3}$, $\gamma = 0.04 \text{ N m}^{-1}$ with various μ_d (cp), for $\theta_0 = 90^\circ$

μ_d	Re	Ca	ξ	Eq.(7)	Eq.(8)
1	1000	2.5	3.696	3.676	3.870
2	500	5	3.281	3.276	3.382
5	200	12.5	2.796	2.814	2.827
10	100	25	2.462	2.508	2.468
100	10	250	1.714	1.711	1.567

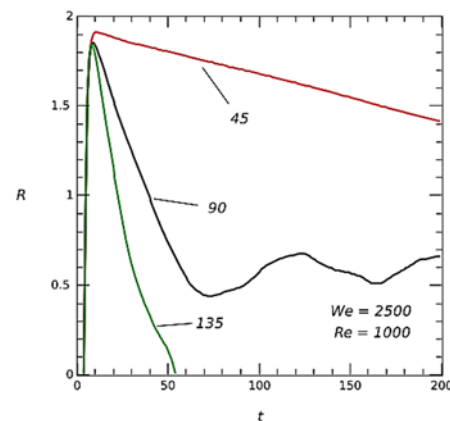


Fig. 6. Plot of R versus t , as in Fig. 5, with $\mu_d = 1$ cp, but for $\theta_0 = 45^\circ$, 90° , and 135° , as labeled.

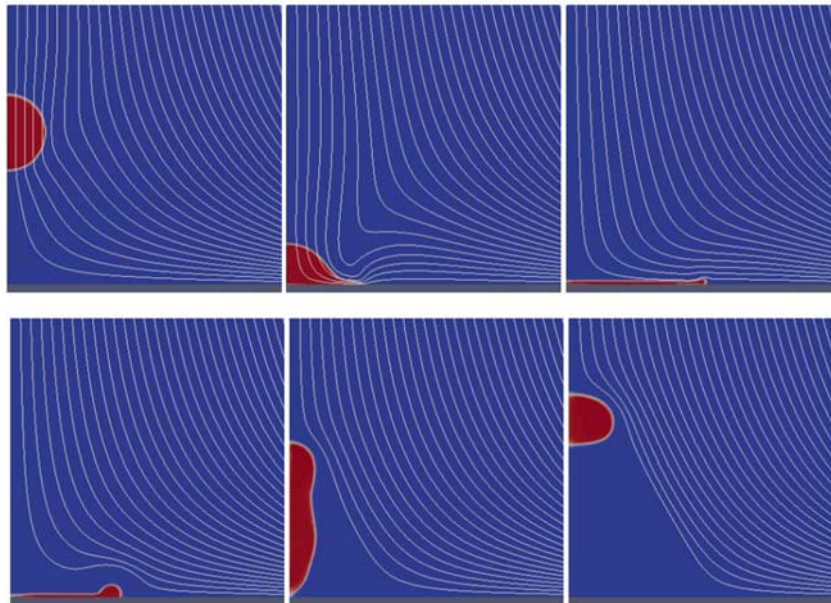


Fig. 7. Streamlines associated with a droplet impact at $Re = 1000$ and $Ca = 2.5$ ($We = 2500$ and $Oh = 0.05$, as in Fig. 2), but for contact angle $\theta_0 = 135^\circ$ ($\theta_A = 140^\circ$, $\theta_R = 130^\circ$) for spreading at $t = 3, 5, 8$ in the upper row, and receding to bouncing at $t = 15, 51$, and 80 in the lower row.

To test the validity of (7) and (8) for contact angles other than $\theta_0 = 90^\circ$, computations of cases for $\theta_0 = 45^\circ$ (with $\theta_A = 50^\circ$ and $\theta_R = 40^\circ$) while other parameters remain unchanged from those in Table 1 are also performed. The results show that $\zeta = 3.827$ for $\mu_d = 1$ cp ($Oh = 0.05$), 3.396 for 2 cp ($Oh = 0.1$), 2.849 for 5 cp ($Oh = 0.25$), 2.484 for 10 cp ($Oh = 0.5$), and 1.724 for 100 cp ($Oh = 5$), with a spreading time $\approx 6.5 \times d/U$ ($= 0.325 \mu s$) which is about $0.1 \mu s$ longer than the case of $\theta_0 = 90^\circ$. Results for $\theta_0 = 135^\circ$ (with $\theta_A = 140^\circ$ and $\theta_R = 130^\circ$) show that $\zeta = 3.624$ for $\mu_d = 1$ cp, 3.231 for 2 cp, 2.782 for 5 cp, 2.448 for 10 cp, and 1.705 for 100 cp, with a spreading time $\approx 3.5 \times d/U$ ($= 0.175 \mu s$). Hence, the computed values of ζ (at $We = 2500$) are indeed insensitive to the contact angle variations, as consistent with the experimental findings of Scheller and Bousfield (1995).

However, the contact angle may drastically influence the dynamics of free surface deformation after the completion of spreading phase (as described by Rioboo *et al.*, 2002). Fig. 6 shows that a droplet with contact angle $\theta_0 = 45^\circ$ (at $Re = 1000$ and $Ca = 2.5$) recedes very slowly in contrast to the case of $\theta_0 = 90^\circ$ with considerable oscillations after receding, while the droplet with $\theta_0 = 135^\circ$ recedes rapidly with great momentum such that it bounces off the solid surface (around $t = 51$).

Physically, bouncing can occur when kinetic energy of impact remains sufficiently large in the receding phase if the viscous dissipation effect is relatively weak such that the shrinking lamella contact line virtually disappears near the impact point (Yarin, 2006). Fig. 7 shows the snapshots of such free surface shape evolution from spreading to receding-bouncing, with streamlines being also displayed to illustrate external gas flow field interaction with the

free surface deformation at different stages. Clearly, the liquid droplet impact dynamics can influence the external gas flow significantly. In view of the flow streamlines, the droplet, having about the same velocity as the surrounding gas at $t = 0$, moves ahead the decelerating gas due to its inertia as it approaches the substrate at $t = 3$. The fast moving liquid droplet tends to drag nearby gas at an increased local velocity during the spreading phase, e.g., at $t = 5$. Toward the end of droplet spreading, e.g., at $t = 8$, as the liquid phase motion diminishes, the gas phase around free surface recovers its natural impinging jet type of flow structure. During the relatively slow receding process, e.g., at $t = 15$ a somewhat stagnant zone in the gas phase develops near the free surface. As the droplet leaving the substrate during bouncing, a low velocity wake appear behind it, e.g., at $t = 51$ and 80 . The bouncing droplet is moving against a gas jet flow that tends to push it back toward the substrate. Thus, the bouncing droplet will eventually come back to reattach to the substrate with the impinging jet flow.

An examination of the effect of liquid viscosity μd for a droplet with contact angle $\theta_0 = 135^\circ$ indicates that the dynamics after spreading is also controlled by the value of Reynolds number Re . Fig. 8 shows that receding momentum decreases with increasing μd (namely, reducing Re), and bouncing would not occur when $Re = 250$ (for R never reaches zero). At $Re = 333$ the droplet detaches from the substrate around $t = 93$, but reattaches to the substrate around $t = 143$ for lack of bouncing momentum. Reducing Re tends to increase the time from the droplet impact to its detaching from substrate, if bouncing occurs. For example, a droplet with $Re = 1000$ impacts the substrate at $t = 4.5$ and detaches from the substrate at $t \approx 53$, with $Re = 500$ at $t \approx 63$, and

with $Re = 333$ at $t \approx 96$. As expected, liquid viscosity has an effect of retarding the free surface flow during receding bouncing.

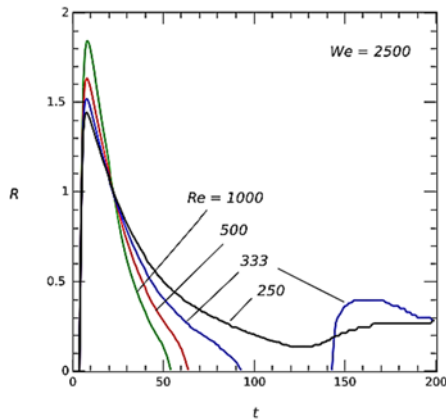


Fig. 8. Plot of R versus t , as in Fig. 6, with $\mu_d = 1, 2, 3,$ and 4 cp, for $\theta_0 = 135^\circ$.

If a droplet of $d = 5 \mu\text{m}$ with viscosity $\mu_d = 1$ cp has a density $\rho_d = 4000 \text{ kg m}^{-3}$ and surface tension $\gamma = 0.08 \text{ N m}^{-1}$, the values of Re and Ca for $U = 100 \text{ m/s}$ become 2000 and 1.25, which lead to $We = 2500$ and $Oh = 0.025$. The computed ζ now becomes 4.177, while (7) and (8) predict 4.124 and 4.4267, respectively. This may be considered as an extreme case for relatively weak droplet viscous effect compared to the inertial and surface tension effects in Aerosol Jet[®] ink droplet deposition. Because of the reduced viscous effect, enhanced free surface deformations and opportunity for bouncing can be observed even at $\theta_0 = 90^\circ$.

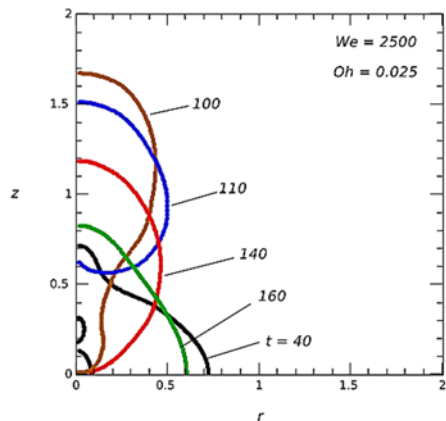


Fig. 9. Detaching and reattaching: as in Fig. 2 but for $\rho_d = 4000 \text{ kg m}^{-3}$ and surface tension $\gamma = 0.08 \text{ N m}^{-1}$ ($Re = 2000$ and $Ca = 1.25$, or $We = 2500$ and $Oh = 0.025$) with $\theta_0 = 90^\circ$ at $t = 40, 100, 110, 140,$ and 160 .

Figure 9 shows a phenomenon of detaching and reattaching, after a droplet impact for $Re = 2000$ and $Ca = 1.25$ (or $We = 2500$ and $Oh = 0.025$) with $\theta_0 = 90^\circ$. Entrapped bubbles can be seen to form during the receding phase, as indicated in the free surface profile at $t = 40$. The center height H reaches its peak value 1.779 at $t = 83$. The contact radius R shrinks to zero at $t = 106$ corresponding to

the time for complete detachment of the droplet from substrate, when the free surface pinches off at the end of a tail formed at the droplet bottom (cf. the free surface profile at $t = 100$). The tip of such tail moves rapidly upward into the bulk of the droplet, due to the action of surface tension, leaving a deep dimple on the droplet bottom at $t = 110$. While moving downward and oscillating with a considerable amplitude, the bottom of the detached droplet reattaches the substrate at $t = 140$. Thereafter, the attached droplet exhibits oscillatory motions with larger amplitudes than that in Fig. 4, as a consequence of stronger effects of fluid inertia and surface tension.

3.2 Cases of $We = 100$

If the droplet of $d = 5 \mu\text{m}$, $\rho_d = 2000 \text{ kg m}^{-3}$, $\mu_d = 1$ cp, and $\gamma = 0.04 \text{ N m}^{-1}$ has an impact velocity of 20 m/s, the values of Re and Ca become 200 and 0.5 such that $We = 100$ and $Oh = 0.05$. The spreading time for $We = 100$ is around $t = 2.0$, corresponding to a dimensional time of $\approx 2.0 \times d/U$ ($= 0.5 \mu\text{s}$ for $d = 5 \mu\text{m}$ and $U = 20 \text{ m/s}$), which seems to be consistent with the experimental findings of drop impact scaling time $t \times d/U \propto We^{-0.25}$ by Antonini *et al.* (2012).

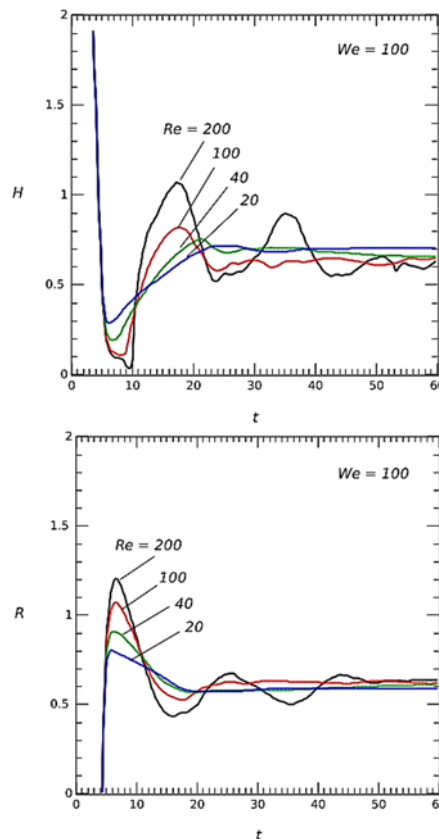


Fig. 10. As in Fig. 5, but at $U = 20 \text{ m/s}$ ($We = 100$) with t in units of $d/U = 0.25 \mu\text{s}$.

The effect of increasing liquid viscosity μ_d on dynamics of a droplet of $d = 5 \mu\text{m}$, $\rho_d = 2000 \text{ kg m}^{-3}$, and $\gamma = 0.04 \text{ N m}^{-1}$ with $U = 20 \text{ m/s}$ is shown in Fig. 10 for the center height H and contact radius R versus t . It is interesting to note that the curves in

Fig. 10 are quite similar to those in Fig. 5 corresponding to the same values of Oh , despite more than an order of magnitude reduction of We . Be-cause there is a factor of 5 difference in the reference time scale d/U (due to a factor of 5 reduction of U), $t = 60$ in Fig. 10 has the same dimensional time $15 \mu s$ $t = 300$ in Fig. 5. This is expected in view of the fact that the impact velocity U only pro-vides the initial free surface deformation that sets the droplet into free oscillatory motion, the characteristics of which is actually determined by ρ_d , d , and γ (Landau and Lifshitz, 1959). Noteworthy here is that Oh ($\equiv \mu_d / \sqrt{\rho_d \gamma d}$) is independent of U , unlike Re , Ca , and We . The fluid viscosity contained in Oh is responsible for the decay of oscillation amplitude, whereas ρ_d , d , and γ are the key ingredients for capillary driven oscillations. Similar to the case of $We = 2500$, the oscillatory motion seems to also diminish for $Oh > 0.25$ at $We = 100$.

Similar to that shown in Fig. 5, H decrease with t after impaction. But the lamella at $We = 100$ is thicker (with larger H_{min}) than that for the same value of Oh at $We = 2500$. For example, the values of H_{min} are reached as 0.0353 at $t = 9.6$ for $Re = 200$, 0.1097 at $t = 7.8$ for $Re = 100$, 0.1940 at $t = 6.8$ for $Re = 40$, and 0.2881 at $t = 6.2$ for $Re = 20$ and 500, respectively. While the oscillatory characteristics following the spreading phase appear independent of U (and We), the thickness of the spreading lamella as well as ζ are strongly influenced by the value of We .

The computed values of ζ for $We = 100$ at various Re corresponding to various values of μ_d for droplets of $d = 5 \mu m$, $\rho_d = 2000 \text{ kg m}^{-3}$, $\gamma = 0.04 \text{ N m}^{-1}$ with $U = 20 \text{ m/s}$ are given in Table 2, along with that of (7) and (8). Again, the agreement is quite reasonable. It should be noted that the value of ζ for the case of $\mu_d = 100 \text{ cp}$ ($Re = 2$) is actually smaller than that at capillary equilibrium for $\theta_0 = 90^\circ$ (namely, 1.26). The value of ζ in this case may not be literally regarded as the “maximum spread factor”. What is given here is actually the peak value of the spread factor $2R$ marking the end of the rapid spreading phase. In this case, R may decrease slightly for a while from its peak value in the relaxation phase, and then slowly increases to-ward its capillary equilibrium value 0.63.

**Table 2 As in Table 1, but at $We = 100$
($U = 20 \text{ m/s}$)**

μ_d	Re	Ca	ζ	Eq.(7)	Eq.(8)
1	200	0.5	2.415	2.154	2.594
2	100	1	2.149	1.920	2.291
5	40	2.5	1.819	1.649	1.938
10	20	5	1.606	1.470	1.705
100	2	50	1.143	1.003	1.103

To check the validity of (7) and (8) for contact angles other than $\theta_0 = 90^\circ$, cases for $\theta_0 = 45^\circ$ and 135° (while other parameters remain unchanged

from those in Table 2) are also computed. The results show that $\zeta = 2.647$ and 2.272 for $\mu_d = 1 \text{ cp}$ ($Oh = 0.05$), 2.293 and 2.064 for 2 cp ($Oh = 0.1$), 1.905 and 1.796 for 5 cp ($Oh = 0.25$), 1.632 and 1.596 for 10 cp ($Oh = 0.5$), and 1.143 and 1.143 for 100 cp ($Oh = 5$). A trend seems to indicate diminishing difference between the values of ζ for $\theta_0 = 45^\circ$ and 135° with increasing Oh which is a measure of relative strength of the viscous effect. In general, the computed values of ζ (at $We = 100$) are insensitive to the contact angle variations, as consistent with the findings of Scheller and Bousfield (1995) and reasoning of Rioboo *et al.* (2002) for insignificant influence of contact angle to ζ .

However, the dynamics of free surface flow after initial spreading can be quite sensitive to the contact angle for $We = 100$, similar to that shown for $We = 2500$. A droplet with $\theta_0 = 45^\circ$ recedes very slowly whereas the contact line of that with $\theta_0 = 135^\circ$ moves rapidly during receding such that bouncing can occur. Noteworthy here is that the same droplet of $d = 5 \mu m$, $\rho_d = 2000 \text{ kg m}^{-3}$, $\gamma = 0.04 \text{ N m}^{-1}$ with viscosity $\mu_d = 5$, ($Oh = 0.25$) and $\theta_0 = 135^\circ$ would bounce (i.e., detach) from substrate at $t = 26.8$ for $U = 20 \text{ m/s}$ ($We = 100$) but remain attached to the substrate at $U = 100 \text{ m/s}$ ($We = 2500$, as indicated in Fig. 8). This appears to be consistent with the trend shown by Durickovic and Varland (2005) for water drop impact on a solid surface and by Law (2015) in a general description of droplet impact dynamics that bouncing is expected at lower We .

3.3 Cases of $We = 5$

For a relatively small droplet of $d = 1 \mu m$, $\rho_d = 1000 \text{ kg m}^{-3}$, $\mu_d = 1 \text{ cp}$, and $\gamma = 0.08 \text{ N m}^{-1}$ with $U = 20 \text{ m/s}$, the values of Re and Ca become 20 and 0.25 such that $We = 5$ and $Oh = 0.1118$. For the same values of Re and Ca , we can compute solutions with the same (dimensional) OpenFOAM mesh for $d = 5 \mu m$, $\rho_d = 200 \text{ kg m}^{-3}$, $\mu_d = 1 \text{ cp}$, and $\gamma = 0.08 \text{ N m}^{-1}$ with $U = 20 \text{ m/s}$.

Figure 11 shows the variations of droplet surface pro-file with time for $We = 5$ and $Oh = 0.1118$. In contrast to Figs. 2—4 for $We = 2500$ and $Oh = 0.05$, the droplet surface in Fig. 11 does not form a commonly observed thin lamella with a bulged rim formed at the beginning of receding phase ($t = 5.6$) due to lack of impact momentum. The maximum contact radius at $t = 5.6$ is 0.6995 while the center height reaches its minimum value of 0.4571,(which is much larger than 0.0266 for $We = 2500$ and $Oh = 0.05$). Following the end of spreading phase, the contact radius recedes and then oscillates with a small amplitudes. Increasing liquid viscosity μ_d , for a droplet of $d = 5 \mu m$, $\rho_d = 200 \text{ kg m}^{-3}$, and $\gamma = 0.08 \text{ N m}^{-1}$ with $U = 20 \text{ m/s}$, further reduces the magnitude of free surface deformations. The value of R could not even reach its capillary equilibrium value during the spreading phase for $\mu_d \geq 5 \text{ cp}$ ($Oh \geq 0.5590$); rather it slowly creeps toward 0.63 in the lengthy wetting equilibrium phase. However, even for the case of $\mu_d = 10$ ($Oh = 1.1180$) the center height H still exhibits noticeable oscillatory motions, because of weaker viscous damping effect in the thick lamella away from the solid wall.

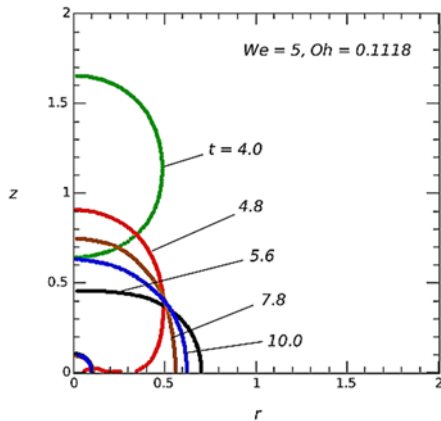


Fig. 11. As in Fig. 2 but for $\rho_d = 200 \text{ kg m}^{-3}$, $\mu_d = 1 \text{ cp}$, and $\gamma = 0.08 \text{ N m}^{-1}$ ($Re = 20$ and $Ca = 0.25$, or $We = 5$ and $Oh = 0.1118$) with $\theta_0 = 90^\circ$ at $t = 4.0, 4.8, 5.6, 7.8,$ and 10.0 .

If the liquid viscosity μ_d is increased to 10 cp ($Re = 2$ and $Ca = 2.5$), the receding and oscillation phase disappears, with R increasing monotonically with time t as shown in Fig. 12. However, there still seems to be a spreading phase corresponding to a rapid increase of R , i.e., with a relatively large dR/dt , followed by a relaxation phase with diminishing dR/dt toward capillary equilibrium $R \approx 0.63$. Because there are no local extrema for R , the end of spreading phase cannot be clearly defined. The fact that the profile at $t = 10.0$ with a monotonically increasing contact radius R has a center height H slightly greater than that at $t = 5.6$ around the end of spreading suggests an ensuing oscillation of the free surface.

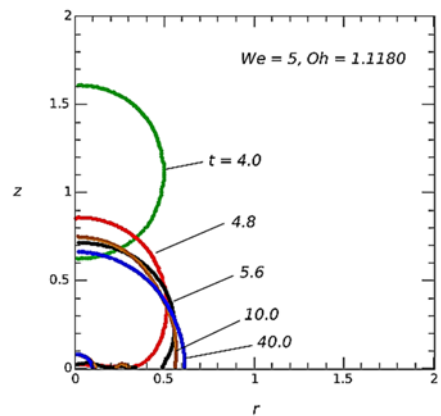


Fig. 12. As in Fig. 11 but for $\mu_d = 10 \text{ cp}$ ($Re = 2$ and $Ca = 2.5$, or $We = 5$ and $Oh = 1.1180$) at $t = 4.0, 4.8, 5.6, 10.0,$ and 40.0 .

Table 3 shows the computed ζ for $We = 5$ at various Re with various values of μ_d for droplets of $d = 5 \text{ }\mu\text{m}$, $\rho_d = 200 \text{ kg m}^{-3}$, and $\gamma = 0.08 \text{ N m}^{-1}$ at $U = 20 \text{ m/s}$, along with that of (7) and (8). Again, the agreement is generally reasonable. For cases of $Re \leq 4$, the value of ζ is taken as the (normalized) contact diameter at the end of spreading phase rather than literally the maximum contact diameter. However, the end of spreading phase may not be clearly defined. At $Re = 4$, a local extremum (or

peak) of R exists; so such a local peak value of R is used for calculating ζ . But for $Re = 2$ and 0.2 , $R(t)$ increases monotonically without local extrema; the end of spreading phase can only be estimated based on the slope change. These estimated ζ in Table 3 are marked by an approximation sign (\sim).

Table 3 As in Table 1, but at $We = 5$ ($U = 20 \text{ m/s}$), for droplets of $d = 5 \text{ }\mu\text{m}$, $\rho_d = 200 \text{ kg m}^{-3}$, (or equivalently $d = 1 \text{ }\mu\text{m}$, $\rho_d = 1000 \text{ kg m}^{-3}$), $\gamma = 0.08 \text{ N m}^{-1}$

μ_d	Re	Ca	ζ	Eq.(7)	Eq.(8)
1	20	0.25	1.399	1.146	1.302
2	10	0.5	1.285	1.022	1.192
5	4	1.25	≈ 1.12	0.878	1.047
10	2	2.5	≈ 1.05	0.782	0.942
100	0.2	25	≈ 0.84	0.534	0.643

If computations are performed for cases of $We = 5$ with θ_0 other than 90° (while other parameters remain unchanged from those in Table 3), the results for ζ seems to still be reasonably close to those for $\theta_0 = 90^\circ$, especially when μ_d is large. For example, with $\theta_0 = 135^\circ$ for $\mu_d = 5 \text{ cp}$ ($Oh = 0.5590$) and 10 cp ($Oh = 1.1180$) a local extremum appears with the peak value of contact radius $R_{max} = 0.503$ or $\zeta = 1.006$ and $R_{max} = 0.469$ or $\zeta = 0.938$, which are especially close to predicted values of 1.047 and 0.942 by (8). The value of ζ remains the same at 0.835 for the case of $\mu_d = 100 \text{ cp}$ ($Oh = 11.1803$) at $\theta_0 = 135^\circ$. But for $\mu_d = 1 \text{ cp}$ ($Oh = 0.1118$) and $\mu_d = 2 \text{ cp}$ ($Oh = 0.2236$), the values of R_{max} for $\theta_0 = 135^\circ$ become 0.5985 or $\zeta = 1.1970$ and 0.5558 or $\zeta = 1.1116$, which are more than 10% off the corresponding values in Table 3 for $\theta_0 = 90^\circ$. Similarly with $\theta_0 = 45^\circ$ and $\mu_d = 1$, the computed $\zeta = 1.656$ is $\sim 18\%$ off 1.399 in Table 3. Hence, the effect of contact angle θ_0 on maximum spread factor ζ seems to become more noticeable at small values of We (e.g., $We < 10$), especially for less viscous droplets.

As shown with the cases of $We = 2500$ and 100 , bouncing tends to occur for droplet impact onto a hydrophobic surface. However, for $We = 5$ with $\theta_0 = 135^\circ$, droplet bouncing after impact only happens when the liquid viscosity is very low, e.g., $\mu_d = 1 \text{ cp}$ ($Re = 20$). Thus, the simple trend of bouncing at relatively smaller We (e.g., Durickovic and Varland, 2005; Law, 2015) may not be general enough to cover all cases. For example, the obvious effect of liquid viscosity on the likelihood of bouncing illustrated in Fig. 8 cannot be explained by considering the Weber number alone.

4. DISCUSSION

Generally speaking, (7) and (8) seem to describe the maximum spread factor ζ fairly accurately over a wide range of parameters for high-speed microdroplet impact, with (8) being slightly more favorable in comparison with the present results. Noteworthy here is that many different empirical,

semiempirical formulas were proposed in the literature, with substantial discrepancies among each other (as illustrated by Perelaer *et al.*, 2009; Ravi *et al.*, 2010; Visser *et al.*, 2012, 2015). After comparing with several of the available formulas, (7) and (8) are selected because their agreement with the present results appears to be quite consistent across the ranges of parameters relevant to Aerosol Jet® printing. However, neither (7) nor (8) explicitly accounts for the contact angle effect, which tends to become more noticeable with reduced We and small Ca (e.g., $We = 5$ and $Ca < 1$). Unlike (7) and (8), the formula derived by Pasandideh-Fard *et al.* (1996) based on energy balance contains the contact angle θ_0 as

$$\xi = \sqrt{\frac{12 + We}{3(1 - \cos\theta_0) + 4\sqrt{CaWe}}} \quad (9)$$

Despite its discrepancy from our computed ξ , (9) indeed suggests that the effect of θ_0 diminishes when $Ca \times We$ becomes close to 100 or greater. It also predicts the trend of decreasing θ_0 effect on ξ with increasing Ca (or μ_d) as consistent with the present results. In view of the general accuracy of (8) and reasonable account for the trend of contact angle effect with (9), a straightforward combination of the two yields

$$\xi = \left(Re^{1/5} - 0.35 \frac{Re^{2/5}}{\sqrt{We}} \right) \times \sqrt{\frac{3 + 4\sqrt{CaWe}}{3(1 - \cos\theta_0) + 4\sqrt{CaWe}}} \quad (10)$$

For example, in the case of a droplet with $d = 1 \mu\text{m}$, $\rho_d = 1000 \text{ kg m}^{-3}$, $\gamma = 0.08 \text{ N m}^{-1}$, and $\mu_d = 1 \text{ cp}$ impacting the substrate at $U = 20 \text{ m/s}$ ($We = 5$ and $Ca = 0.25$) and $\theta_0 = 135^\circ$, the computed $\xi = 1.197$ and that from (10) is 1.149 whereas 1.302 from (8). If μ_d is increased to 2 cp ($We = 5$ and $Ca = 0.5$), the computed $\xi = 1.112$ and that from (10) is 1.076 whereas 1.192 from (8). With $\theta_0 = 45^\circ$ for $\mu_d = 1$ and 2 cp ($Ca = 0.25$ and 0.5), the computed ξ are 1.656 and 1.379 while that from (10) are 1.539 and 1.356, much improved from 1.302 and 1.192 by (8). Thus, (10) can be a useful formula with improved accuracy for the range of parameters of interest to the Aerosol Jet® direct-write technology.

While ξ provides a practically useful correlation between the Feret diameter of deposited individual droplets on a dry substrate and the droplet diameter d , other dynamic outcomes of droplet impact can be relevant to Aerosol Jet® ink deposition, too. Although not computed with the present axisymmetric model, the splashing phenomenon usually observed in droplet impact with large We and Re is also of great importance to Aerosol Jet® printing for being a possible source of undesirable over-sprays and uncontrolled satellites. Historically, the first study of splashing after droplet impact was carried out by Worthington (1876). Splashing of large milk and mercury droplets onto smooth glass

plates was observed and the corresponding fingering pat-terns were sketched, with the number of fingers increasing with both droplet size and fall height being noted. Several investigations on surface roughness effect on splashing behavior suggested that splashing at atmospheric pressure only occurs when

$$K \equiv \frac{We}{Oh^{2/5}} > K_s \text{ with } K_s = 649 + \frac{3.76}{R_a^{0.63}}, \quad (11)$$

where R_a denotes the nondimensional roughness parameter in units of d (Stow and Hadfield, 1981; Mundo *et al.*, 1995; Cossali *et al.*, 1997; Yarin, 2006). Thus, $K_s \rightarrow 649$ as $R_a \rightarrow \infty$ for a very rough surface, whereas K_s increases to infinity as $R_a \rightarrow 0$ for an extremely smooth surface. However, other forms for splashing criteria had also been proposed in the literature (e.g., Moreira *et al.*, 2010; Mandre and Brenner, 2012; Stevens, 2014), but little agreement had been shown among different criteria which often contradict one another (Visser *et al.*, 2015). While careful examining the validity of each proposed criterion is out of scope of the present work, (11) may be used as a tentative reference for a brief discussion here.

For Aerosol Jet® ink droplets of $d = 5 \mu\text{m}$, $R_a = 0.1$ (which leads to $K_s = 665$, only slightly greater than 649) corresponds to a roughness length scale ($0.5 \mu\text{m}$) around the wavelengths of visible light which is usually considered as a fairly smooth surface with most of realistic substrate surfaces. For cases with $U = 100 \text{ m/s}$ ($We = 2500$), as those in Table 1, the values of K are all exceeding 649 (or 665), ranging from 1313 for $Re = 10$ to 8286 for $Re = 1000$. Thus, when operating at a very high jet® speed (e.g., $U = 100 \text{ m/s}$) under atmospheric pressure, the Aerosol Jet® ink droplets of $d = 5 \mu\text{m}$ are expected to disintegrate as a consequence of splashing after impacting the substrate. If the ink droplet d is reduced to $2 \mu\text{m}$ with $\mu_d = 100 \text{ cp}$ at the same U , the value of K can become 437 (< 649). Even for an ink droplet of $d = 1 \mu\text{m}$ with $\mu_d = 5 \text{ cp}$ (for $\rho_d = 2000 \text{ kg m}^{-3}$ and $U = 100 \text{ m/s}$), the value of K is 631, barely below the reference splashing thresh-old value 649. Thus, to avoid ink droplet splashing upon deposition in Aerosol Jet® printing with high-speed jet, it is preferable to keep the droplet size small and viscosity high (which may be accomplished by enabling effective in-flight mist solvent evaporation).

5. CONCLUDING REMARKS

In view of the challenges with required high spatial and temporal resolutions for experimentally analyzing the ink droplet deposition behavior during Aerosol Jet® printing (with microdroplets of $d = 1$ to $5 \mu\text{m}$ and $U = 20$ to 100 m/s), numerical solutions for high-speed microdroplet impact perpendicularly onto a smooth solid surface are computed in the present work using the *interFoam* VoF solver of the OpenFOAM® CFD package. The computed

results illustrate droplet impact dynamics with lamella shape evolution throughout the spreading, receding-relaxation, and wetting equilibrium phases, consistent with what have been observed and described in various previous studies. This fact agrees with the conclusions of Visser *et al.* (2015) that the basic droplet impact behavior is scale-invariant; in other words, experiments with larger droplets at the same nondimensional parameter values should be able to describe the phenomena with much smaller droplets. When the droplet viscosity is relatively low, significant oscillations in the free-surface flow can be observed. But the free surface oscillatory motion seems to diminish as the droplet viscosity μ_d becomes relatively high. The border line between periodic free surface oscillations and aperiodic creeping to the shape of capillary equilibrium following spreading appears at Oh ($\equiv \mu_d / \sqrt{\rho_d \gamma d}$) about 0.25.

The computed results show that substrate surface properties such as the contact angle can drastically influence the dynamics of free surface deformation after the spreading phase. For example, droplet bouncing (i.e., rebound) is prompted with large contact angles at solid surface (i.e., hydrophobic surface, consistent with findings reported by Rio-boo *et al.*, 2001; Durickovic and Varland, 2005), but its likelihood can be reduced by increasing the droplet viscosity due to enhanced kinetic energy dissipation. At some intermediate viscosity values, reattachmet of the bouncing droplet to the solid surface can be observed within a short time. When using a high-speed jet flow to direct the ink droplet deposition in Aerosol Jet® printing, droplet bouncing after impact on substrate is generally undesirable for causing unintended ink placement such as “satellite”, “overspray”, etc.

Special attention has been paid to the value of maximum spread factor ζ , which can be accurately determined from the numerical solutions. For the range of parameters of practical interest to the Aerosol Jet® printing, the values of computed ζ agree quite well with the empirical correlation of Scheller and Bousfield (1995) based mostly on experimental data and the semiempirical relation proposed by Roisman (2009) based on an analytical theory for inertia dominated situations (with a slight modification of the coefficient values). Majority of the computed cases show insignificant variations of ζ with changes of contact angle θ_0 , as expected when the inertial effect dominates the spreading dynamics. The weak dependence of ζ on θ_0 , more noticeable at relatively small Ca and We , can be accounted for with a straightforward modification of a combined formulas of Pasandideh-Fard *et al.* (1996) and Roisman (2009). The resulting formula of maximum spread factor can be used for first-order evaluations of the Feret diameter of deposited individual ink droplets for Aerosol Jet® technology development.

ACKNOWLEDGMENTS

The author would like to thank John Lees for encouragement and guidance, and Dr. Mike Renn for insightful discussion.

REFERENCES

- Alavi, S., M. Passandideh-Fard and J. Mostaghimi (2012). Simulation of semi-molten particle impacts including heat transfer and phase change. *J. Therm. Spray Tech.* 21(6), 1278-1293.
- Antonini, C., A. Amirfazli and M. Marengo (2012). Drop impact and wettability: From hydrophilic to superhydrophobic surfaces. *Phys. Fluids* 24, 102104
- Attane, P., F. Girard and V. Morin (2007). An energy balance approach of the dynamics of drop impact on a solid surfaces. *Phys. Fluids* 19, 012101
- Berberovic, E., N. P. Van Hinsber, S. Jakirlic, I. V. Roisman and C. Tropea (2009). Drop impact onto a liquid layer of finite thickness: Dynamics of the cavity evolution. *Phys. Rev. E* 79(3), 036306
- Bussmann, M., J. Mostaghimi and S. Chandra (1999). On a three-dimensional volume tracking model of droplet impact. *Phys. Fluids* 11(6), 1406-1417.
- Bussmann, M., S. Chandra and J. Mostaghimi (2000). Modeling the splash of a droplet impacting a solid surface. *Phys. Fluids* 12(12), 3121-3132.
- Chandra, S. and C. T. Avedisian (1991). On the collision of a droplet with a solid surface. *Proc. R. Soc. London A* 432, 13-41.
- Christenson, K. K., J. A. Paulsen, M. J. Renn, K. McDonald and J. Bourassa (2011). Direct printing of circuit boards using Aerosol Jet®. *Proc. NIP 27 Digital Fabric.* 433-436.
- Cossali, G. E., A. Coghe and M. Marengo (1997). The impact of a single drop on a wetted solid surface. *Exp. Fluids* 22, 463-472.
- Deshpande, S. S., A. Lakshman and M. F. Trujillo (2012). Evaluating the performance of the two-phase flow solver interFoam. *Comput. Sci. Discov.* 5, 04016
- Dinc, M. and D. D. Gray (2012). Drop impact on a wet surface: computational investigation of gravity and drop shape. *Advance in Fluid Mechanics and Heat and Mass Transfer* 374-379.
- Durickovic, B. and K. Varland (2005). *Between bouncing and splashing: water drops on a solid surface*. Applied Mathematics thesis, University of Arizona
- Feng, J. Q. (2010). A deformable liquid drop falling through a quiescent gas at terminal velocity. *J.*

- Fluid Mech.* 658, 438-462.
- Feng, J. Q. (2015). Sessile drop deformations under an impinging jet. *Theor. Comput. Fluid Dyn.* 29, 277-290.
- Foote, G. B. (1974). The water drop rebound problem: dynamics of collision. *J. Atmos. Sci.* 32, 390-402.
- Ford, R. E. and C. G. L. Furnidge (1967). Impact and spreading of spray drops on foliar surfaces. In *Wetting, Soc. Chem. Industry Mono-graph London* 417-432.
- German, G. and V. Bertola (2009). Review of drop impact models and validation with high-viscosity Newtonian fluids. *Atom. Sprays* 19(8), 787-807.
- Gopala, V. R. and B. G. M. van Wachem (2008). Volume of fluid methods for immiscible-fluid and free-surface flows. *Chem. Eng. J.* 141(1), 204-221.
- Gupta, A. and R. Kumar (2010). Droplet impingement and breakup on a dry surface. *Comput. Fluids* 39, 1696-1703.
- Healy, W. M., J. G. Hartely and S. I. Abdel-Khalik (1996). Comparison between theoretical models and experimental data for the spreading of liquid droplets impacting a solid surface. *Int. J. Heat Mass Transfer* 39, 3079-3082.
- Hedges, M., B. King and M. Renn (2007). Direct writing for advanced electronics packaging. www.onboardtechnology.com/pdf_giugno2007/060706.pdf
- Hoang, D. A., V. van Steijn, L. M. Portela, M. T. Kreutzer and C. R. Kleijn (2013). Benchmark numerical simulations of segmented two-phase flows in microchannels using the volume of fluid method. *Comput. Fluids* 86, 28-36.
- Kahn, B. E. (2007). The M3D aerosol jet system, an alternative to inkjet printing for printed electronics. *Organic and Printed Electronics* 1, 14-17.
- Landau, L. D. and E. M. Lifshitz (1959). *Fluid Mechanics*. Addison-Wesley.
- Law, C. K. (2015). Impact dynamics of droplets and jets. ICLASS2015, 13th Int. Conf. Liquid Atom. Spray Syst. Tainan, Taiwan.
- Linder, N., I. V. Roisman, H. Marschall and C. Tropea (2013). Numerical simulations of pinning droplets. ILASS-Europe 2013, 25th Europ. Conf. Liquid Atom. Spray Syst. Chania, Greece.
- Mandre, S. and M. P. Brenner (2012). The mechanism of a splash on a dry solid surface. *J. Fluid Mech.* 690, 148-172.
- Moreira, A. L. N., A. S. Moita and M. R. Pano (2010). Advances and challenges in explaining fuel spray impingement: how much of single droplet impact research is useful?. *Prog. Energy Combust. Sci.* 36, 554-580.
- Morgan, G. C. J. (2013). *Application of the interFoam VoF code to coastal wave/structure interaction*. Ph. D. thesis, University of Bath.
- Mundo, C., M. Sommerfeld and C. Tropea (1995). Droplet-wall collisions: experimental studies of the deformation and breakup process. *Int. J. Multiphase Flow* 21, 151-173.
- Pasandideh-Fard, M., Y. M. Qiao, S. Chandra and J. Mostaghimi (1996). Capillary effects during droplet impact on a solid surface. *Phys. Fluids* 8, 650-659.
- Paulsen, J. A., M. Renn, K. Christenson and R. Plourde (2012). Printing conformal electronics on 3D structures with Aerosol Jet technology. In *Proceeding of Future of Instrumentation International Work-shop (FIIW)*.
- Perelaer, J., P. J. Smith, E. van den Bosch, S. S.C. van Grootel, P. H. J. M. Ketelaars and U. S. Schubert (2009). The spreading of inkjet-printed droplets with varying polymer molar mass on a dry solid substrate. *Macromol. Chem. Phys.* 210, 495-502.
- Ravi, V., M. A. Jog and R. M. Manglik (2010). Effects of interfacial and viscous properties of liquids on drop spread dynamics. In *Proceeding of ILASS2010-142, 22nd Ann. Conf. Liquid Atom. Spray Syst.* Cincinnati, OH
- Rein, M. (1993). Phenomena of liquid drop impact on solid and liquid surfaces. *Fluid Dyn. Res.* 12, 61-93
- Renn, M. J. (2006). Direct Write™ system. US Patent 7,108,894 B2
- Renn, M., M. Essien, B. H. King and J. A. Paulsen (2010). Aerodynamic jetting of aerosolized fluids for fabrication of passive structures. US Patent 7,674,671 B2
- Rioboo, R., C. Tropea and M. Marengo (2001). Outcomes from a drop impact on solid surfaces. *Atom. Sprays* 11, 155-165.
- Rioboo, R., M. Marengo and C. Tropea (2002). Time evolution of liquid drop impact onto solid, dry surface. *Exp. Fluids* 33, 112-124
- Roisman, I. V. (2009). Inertia dominated drop collisions. II. An analytical solution of the Navier-Stokes equations for a spreading viscous film. *Phys. Fluids* 21, 052104
- Rusche, H. (2002). *Computational fluid dynamics of dispersed two-phase flows at high phase fractions*. Ph. D. thesis, University of London. Imperial College.
- Saha, A. A. and S. K. Mitra (2009). Effect of dynamic contact angle in a volume of fluid (VoF) model for a microfluidic capillary flow. *J. Colloid Interf. Sci.* 339, 461-480.
- Scheller, B. L. and D. W. Bousfield (1995). Newtonian drop impact with a solid surface. *AIChE J.* 41, 1357-1367.

- Sikalo, S., M. Marengo, C. Tropea and E. N. Ganic (2002). Analysis of impact of droplet on horizontal surfaces. *Exp. Therm. Fluid Sci.* 25, 503–510
- Stevens, C. S. (2014). Scaling of the splash threshold for low viscosity fluids. *Europhys. Lett.* 106, 24001
- Stow, C. D. and M. G. Hadfield (1981). An experimental investigation of fluid flow resulting from the impact of a water drop with an unyielding dry surface. *Proc. R. Soc. Lond. A* 373, 419-441.
- Tanner, L. H. (1979). The spreading of silicone oil drops on solid surfaces. *J. Phys. D* 12, 1473-1484.
- Toivakka, M. (2003). Numerical investigation of droplet impact spreading in spray coating of paper. In *Proceedings of TAPPI 8th Advanced Coating Fundamentals Symposium*.
- Ubbink, H. (2002). *Computational Fluid Dynamics of Dispersed Two-Phase Flows at High Phase Fractions*. Ph. D. Thesis, Imperial College of Science, Technology and Medicine, London
- Visser, C. W., P. E. Frommhold, S. Wildeman, R. Mettin, D. Lohse and C. Sun (2015). Dynamics of high-speed microdrop impact: numerical simulations and experiments at frame-to-frame times below 100ns. *Soft Matter* 11, 1708-1722.
- Visser, C. W., Y. Tragawa, C. Sun and D. Lohse (2012). Microdroplet impact at very high velocity. *Soft Matter* 8(41), 10732-10737.
- Worthington, A. M. (1876). On the forms assumed by drops of liquids falling vertically on a horizontal plate. *Proc. R. Soc. Lond.* 25, 261-271.
- Yarin, A. L. (2006). Drop impact dynamics: splashing, spreading, receding, bouncing... *Ann. Rev. Fluid Mech.* 38, 159-192.
- Zollmer, V., M. Muller, M. Renn, M. Busse, I. Wirth, D. Godlinski and M. Kardos (2006). Printing with aerosols: A maskless deposition technique allows high definition printing of a variety of functional materials. *Euro. Coating J.* 07-08,46-55